Catalysis Today 424 (2023) 114303

Contents lists available at ScienceDirect

Catalysis Today

journal homepage: www.elsevier.com/locate/cattod

Genetically evolved graphene encapsulated random alloy nanoparticles for Li-Air battery

Hyunwoo Ha [a,1], Changsoo Lee [b,1], Joon Sik Park [c], Choong-Heui Chung [c], Sangyeob Lee [c], Graeme Henkelman [a], Hyun You Kim [d,*], Kihyun Shin [c,*]

[a] Department of Chemistry and the Oden Institute of Computational Engineering and Sciences, University of Texas at Austin, 100 E 25th Street A5300, Austin, TX 78712, United States
[b] Hydrogen Research Department, Korea Institute of Energy Research, 152 Gajeong-ro, Yuseong-gu, Daejeon 34129, Republic of Korea
[c] Department of Materials Science and Engineering, Hanbat National University, Daejeon 34158, Republic of Korea
[d] Department of Materials Science and Engineering, Chungnam National University, Daejeon 34134, Republic of Korea

ARTICLE INFO

Keywords:
DFT
Li-air battery
Nanoparticle
Catalyst
Graphene encapsulation

ABSTRACT

We conducted an extensive investigation into graphene-encapsulated monometallic (Fe, Co, and Ni) and bimetallic random alloy (FeCo, FeNi, and CoNi) systems for their potential application as highly efficient catalysts in Li-air battery technology. Through meticulous calculations and analyses, we identified the Co@C system as the most exceptional catalyst among the monometallic counterparts. This system exhibited particle-type growth of the discharging product along with a moderate intermediate binding energy. Furthermore, employing the powerful genetic algorithm (GA) method, we explored a vast array of approximately 800–1200 structures to unveil stable random alloy systems. Our investigation led us to the discovery of the remarkable FeCo@C catalyst, presenting a Co-rich surface, Despite the elemental dominance on the catalyst surfaces, we observed the binding of intermediates occurring at ensemble sites involving two elements. Notably, the FeCo@C system emerged as the superior catalyst among both monometallic and bimetallic systems. It displayed a pronounced preference for particle-type growth and showcased the weakest binding energy for Li_3O_4, thereby demonstrating exceptional catalytic activity. Additionally, we performed an in-depth analysis comparing the overall potential difference from the reaction energy diagram with the individual potential differences during the Li_2O_2 formation and decomposition sequence. We established the critical significance of comparing individual potential differences in Li-air battery studies to ensure the preservation of detailed information and maintain the predictive power necessary for suggesting novel and efficacious catalysts. In summary, our groundbreaking study provides invaluable insights into the remarkable performance of graphene-encapsulated monometallic and bimetallic catalysts in Li-air batteries. The Co@C catalyst excelled among the monometallic systems, while the FeCo@C catalyst showcased unparalleled activity within both monometallic and bimetallic systems. Our findings underscore the utmost importance of meticulously considering individual potential differences to drive forward the development of highly efficient catalysts for transformative Li-air battery applications.

1. Introduction

In recent years, the world has faced significant challenges related to energy consumption, environmental pollution, and the urgent need for clean and sustainable energy sources. The reliance on fossil fuels as the primary energy source has not only led to the depletion of these finite resources but has also caused severe environmental consequences, including greenhouse gas emissions and air pollution. To mitigate these issues, extensive research efforts have been devoted to exploring alternative energy technologies that can provide efficient and environmentally friendly solutions [1–6] Among the various emerging energy storage systems, lithium-air (Li-air) batteries have gained considerable attention due to their high theoretical energy density, surpassing that of traditional lithium-ion batteries [7–12] Li-air batteries operate on the principle of the reversible electrochemical reaction between lithium and oxygen, with lithium ions combining with oxygen to form lithium

* Corresponding authors.
E-mail addresses: kimhy@cnu.ac.kr (H.Y. Kim), kihyun@hanbat.ac.kr (K. Shin).
[1] These authors contributed equally to this work.

https://doi.org/10.1016/j.cattod.2023.114303
Received 18 June 2023; Received in revised form 26 July 2023; Accepted 28 July 2023
Available online 29 July 2023

peroxide (Li_2O_2) during discharge.

However, the overly stable Li_2O_2 discharge product poses a significant limitation to the efficiency and practicality of Li-air batteries. The formation of highly insulating Li_2O_2 can impede the battery's rechargeability, reduce its capacity, and induce high overpotentials during charge and discharge cycles [13–19] To overcome the challenges associated with overly stable Li_2O_2 formation, researchers have focused on investigating alternative catalysts and materials that can enhance the electrochemical performance of Li-air batteries. Numerous studies have explored different approaches, such as the introduction of transition metal catalysts [20–25], the use of nanostructured materials [26–28], and the incorporation of additives to promote the decomposition of Li_2O_2 and improve the battery's reversibility. These efforts have aimed to develop novel strategies to mitigate the formation of overly stable Li_2O_2, thereby enhancing the overall performance and efficiency of Li-air batteries.

In recent years, nanoparticle-based catalysts [29–34] and carbon encapsulation [35–39] have emerged as promising candidates for addressing the challenges of Li-air batteries. The use of nanoparticles allows for a higher surface area, increased catalytic activity, and improved charge transfer kinetics, leading to enhanced battery performance. Moreover, carbon encapsulation of the catalyst materials provides stability, prevents aggregation, and improves the durability of the catalyst, ensuring prolonged cycling performance. Recent studies have demonstrated the effectiveness of nanoparticle-based catalysts and carbon encapsulation in promoting Li_2O_2 decomposition, reducing overpotentials, and improving the reversibility of Li-air batteries. [20–24].

In this study, we aim to further investigate the potential of graphene-encapsulated catalyst systems, including monometallic (Fe, Co, and Ni) and bimetallic random alloys (FeCo, FeNi, and CoNi), for their application in Li-air batteries. By exploring the catalytic activity of these systems, we strive to contribute to the development of efficient and reliable Li-air battery technologies. We aim to shed light on the potential pathways for overcoming the limitations associated with overly stable Li_2O_2 discharge products and pave the way toward the realization of high-performance Li-air batteries for future energy storage applications.

2. Computational details

We performed the Generalized Gradient Approximation (GGA) level spin-polarized density functional theory (DFT) calculation using the Vienna ab initio simulation package (VASP) [40–43] based on a plane-wave basis set with a cutoff energy of 450 eV. The revised Perdew-Burke-Ernzerhof (RPBE) [44–46] functional was used to describe the electron exchange and correlation of Fe, Co, and Ni elements. For the geometry optimization of the slab model, we proceed with the two-step calculations since we have dealt with ferromagnetic materials known as difficult to stabilize. The first step is spin-unpolarized geometry optimization to produce a basic electronic structure. In the next step, we performed the spin-polarized calculation based on the electronic structure information we calculated from the previous step. We could successfully stabilize the complex slab model composed of Ni, Co, and Fe elements through these two-step optimizations. The Brillouin zone was sampled with 4 × 4 × 1 k-point mesh following the Monkhorst-Pack scheme. The convergence criteria for the electronic and geometry optimizations were 10^{-5} eV and 10^{-2} eV/Å, respectively.

We constructed two different sets of slab models. The first set is the monometallic Fe, Co, and Ni (111) surface of the face-centered cubic (FCC) structure with graphene encapsulation, and the other set is the bimetallic random alloy systems: FeCo, FeNi, and CoNi, which also have (111) surface indices based on FCC structure with graphene encapsulation. (see Fig. 1) The composition of random alloy systems is 50:50. Both have a total of four atomic layers with two frozen bottom layers. They are centered in the 10 Å vacuum along with z-direction to avoid

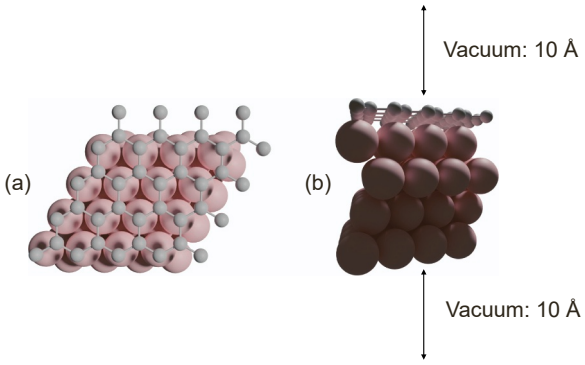

Fig. 1. Illustrations of the slab model we used in this study (a) top view and (b) side view. The ball with gray color represented the encapsulated carbon layer, and the ball with pink color represented any metal elements (Fe, Co, and Ni).

self-interaction. Here, random alloys have been developed from the genetic algorithm (GA) implanted in an atomic simulation environment (ASE). [47,48] We first generated a hundred parents from the random generation as a first generation. Second, we made a hundred children by selecting two parents from the previous generation. Third, keep repeating the evolution until we reached the criteria we set. In this work, we performed at least eight generations (800 structures) until the energy difference hit 10^{-2} eV.

To compare the catalytic activity of Li-air battery, we made the reaction energy diagram for the charging (or oxygen evolution reaction, OER) and discharging (or oxygen reduction reaction, ORR) process, and found the onset potential of both charging and discharging and calculated the potential difference (ΔU) crucial factor in Li-air battery performance. Here is the total reaction pathway.

$$4(Li^+ + e^-) + 2O_2(g) \leftrightarrow 2Li_2O_2(s)$$

The following discharging process was considered; the reversed one could be the charging process.

$$\Delta G_1 : (Li^+ + e^-) + O_2(g) + * \leftrightarrow LiO_2^*$$

$$\Delta G_2 : (Li^+ + e^-) + LiO_2^* \leftrightarrow Li_2O_2^*$$

$$\Delta G_3 : (Li^+ + e^-) + O_2(g) + Li_2O_2^* \leftrightarrow Li_3O_4^*$$

$$\Delta G_4 : (Li^+ + e^-) + Li_3O_4^* \leftrightarrow 2Li_2O_2^*$$

Contrary to the original ORR and OER having proton and electron transfer, we have $Li^+ + e^-$ transfer, and the reference electrode is also based on Li/Li^+ one. Thus, we assume that $Li^+ + e^- \leftrightarrow Li(s)$ are equilibrium at the standard condition to develop computational reference electrode and handle the chemical potential of $Li^+ + e^-$ with $Li(s)$, which is same as computational hydrogen electrode by Nørskov group except we are dealing with Li^+.[49] When we calculate the equilibrium potential and binding energy of a given reaction, we used the energy of Li_2O_2(s) and Li(s) as a reference instead of O_2(g) to match the experimental equilibrium potential (2.96 V vs Li/Li^+) since the DFT has difficulties in dealing with the triplet states of O_2(g).

3. Results and discussion

3.1. The catalytic activity of monometallic nanoparticle

Before investigating which bimetallic system holds the most promise among various element combinations, it is crucial to develop the monometallic system to facilitate comparison and gain insights into the reaction mechanism of simpler systems. In this study, we prepared Fe, Co, and Ni elements with a common face-centered cubic (FCC) structure, despite the possibility of Fe and Co having different stable structures at

room temperature. Adopting the same structure for all elements was motivated by two factors. Firstly, any bimetallic system composed of Fe, Co, and Ni can exhibit an FCC structure in experimental settings [50,51]. Secondly, we assume that the nanoparticle system possesses a high surface-volume ratio, resulting in the synthesis of FCC-structured nanoparticles with (111) surfaces to minimize surface energy. These assumptions enable us to extract key factors underlying changes in catalytic activity with different bimetallic combinations.

To evaluate the binding energies of intermediates (LiO_2, Li_2O_2, and Li_3O_4) that may exist during the reaction, we constructed slab models and performed calculations, as described in the computational details section. Based on the obtained binding energy calculations (Table S1 and Fig. S1), we generated reaction energy diagrams for both discharging (blue) and charging (red) reactions (Fig. 2a-c). Here, we introduced two terminologies: discharging potential (U_{DC}) and charging potential (U_C), similar to concepts such as onset potential or half-wave potential in experimental settings. The onset potential represents the point at which all reaction steps become exothermic. While a direct comparison of onset potential is commonly used to determine catalytic activity, Li-air batteries have different evaluation criteria due to the emphasis on charging efficiency [52–55]. Hence, it is necessary to examine the potential difference to understand the required energy input for recharging. A low potential difference signifies a cost-effective system that demands relatively less energy for recharging. Remarkably, Co@C exhibited the most favorable position among the three early transition metals, namely Fe, Co, and Ni.

However, another critical point is deciding which catalyst performs better in Li-air batteries. According to our previous discussion, the low potential difference made a good catalyst due to the discharging and charging characteristics of the battery. If we determine the potential difference out of entire reactions, we can get the wrong conclusion due to the lost details. In this study, we followed the four reaction steps sequentially from ΔG_1 to ΔG_4 for the discharging process as the reaction happens to make first Li_2O_2 with ΔG_1 and ΔG_2 and second Li_2O_2 with ΔG_3 and ΔG_4, and then the charging process is starting from $\Delta G_{4'}$ to $\Delta G_{1'}$ (here ' means reversed reaction) by evolving O_2(g) from Li_2O_2 in reverse order. (See Fig. S2) Therefore, we must compare the onset potential difference individually such as comparing the first formation of Li_2O_2 (ΔG_1 and ΔG_2) and the first decomposition of Li_2O_2 ($\Delta G_{3'}$ and $\Delta G_{4'}$), and the results were drawn in Fig. 2d-e. As same as the reaction energy diagram, bars with blue color mean discharging process with first (left) and second (right) Li_2O_2 formation in order. In the same manner, bars with red color mean the charging process with the first (right) and second (left) Li_2O_2 decomposition process to compare the potential in sequence. Contrary to our assumption in previous statements, it looks like there is no difference between overall and individual potential differences, however, there is a slight deviation in the Co@C system. The first discharging potential is slightly lower than the second one, thus small difference was observed between Fig. 2b and e in terms of potential difference. Only a 20 mV difference was found in the monometallic system, but bimetallic systems showed dramatic changes that will be discussed later. The Co@C and Ni@C show similar trends they have similar discharging potential, and the first Li_2O_2 decomposition is the main bottleneck of the reaction. The Fe@C shows a big potential difference at the second Li_2O_2 decomposition due to the exceptionally strong binding energy in LiO_2 by − 3.51 eV (the Co@C and Ni@C have the LiO_2 binding energy by 1.13 eV and 1.23 eV, respectively). From the individual potential difference diagram, we still can claim that Co@C shows the best performance among the monometallic systems.

3.2. GA for bimetallic system

From now on, we will discuss bimetallic random alloy systems, however, modeling the random alloy systems even with graphene encapsulation is tricky. Here, we suggest the GA method can find the stable structure given circumstances through the evolution of multiple generations until we find the desired structure. As we discussed briefly in the computational details section. First, we made a hundred structures

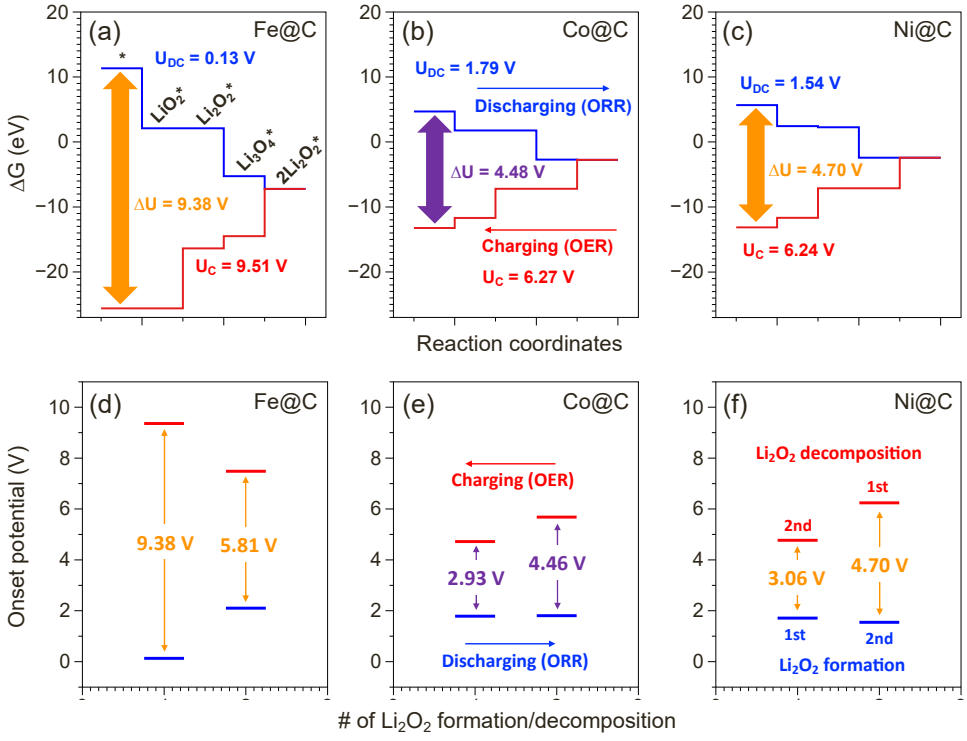

Fig. 2. The reaction energy diagram for charging (blue) and discharging (red) reaction at each onset potential, and potential difference (ΔU) was also represented in orange and purple (lowest) color on the (a) Fe@C, (b) Co@C, and (c) Ni@C. Individual potential differences via sequential reaction on the (d) Fe@C, (e) Co@C, and (f) Ni@C were presented. all the monometallic slab models were encapsulated with the graphene layer.

(so-called parents) from a random shuffle and chose only the metal atoms under the graphene layer that will be evolved via the GA process and performed the DFT calculation. Second, we picked two parents (e.g. A, B) out of a hundred parents, and sliced them at the same angle (e.g. A → A1 +A2, B → B1 +B2), and then rejoin them (e.g. A1 +B2 → C, A2 +B1 = → D) in a different order. These C and D could be the next generation or children. Third, we continued the second process until we got a hundred children and performed the DFT calculation to get the energies of the structures. Forth, we repeated the process over again until the energies hit the criteria we set. Fifth, we chose the ten most stable structures from the GA search and recalculated them with tight criteria for further calculations.

As you can see in Fig. 3, we explored at least eight hundred to fifteen hundred structures to find the stable one. The convergence is clearly seen in every system without any ambiguity. In the case of the FeCo@C system, the Co-rich surface became most stable with small Fe segregation (four atoms on the surface). In other cases, such as FeNi@C and CoNi@C, both systems have Ni-rich surfaces. Especially in an electrochemical environment like a fuel cell, the catalyst surface was fully covered with noble and low surface energy elements like platinum. Interestingly, none of the systems are fully covered with specific elements like Pt-based nanoparticles. [56–58] We believe that graphene encapsulation made the mild condition which can give you more flexibility about the surface configuration than the exposed metal surface. Through the surface structure, we can assume that FeCo@C will have similar properties to the Co@C system but will be slightly tuned by Fe atoms under the graphene. A similar effect can be also expected on the FeNi@C and CoNi@C systems as well. Both will have similar properties to the Ni@C since they have Ni-rich surfaces, but FeNi@C will be tuned by Fe atoms and CoNi@C will be tuned by Co atoms. When we tried to find the most stable binding sites for LiO_2, it always binds on the alloy sites shown in Fig. S3. In other words, unique surface configurations derived by graphene encapsulation may change the catalytic activity of the systems since the first discharging step (LiO_2 binding) can happen on the mixed binding sites. In this section, we explored the vast number of structures for FeCo@C, FeNi@C, and CoNi@C, and found the most stable structures having Co- or Ni-rich surfaces.

3.3. The catalytic activity of the bimetallic system

We calculated the binding energies of intermediates and catalytic activity on the bimetallic random alloy systems investigated from the GA method. As we discussed in the last section about LiO_2 binding, ensemble sites with two elements became reactive. Additional intermediates were also studied, and we found the different types of discharging product (Li_2O_2) growth possibilities. One of the major drawbacks of Li-air batteries is the overly stable Li_2O_2 because it can be a problem of Li_2O_2 decomposition. Zhang reported that there were two different kinds of discharging product growth mechanisms. [59] One is the film-type growth will cover whole catalysts uniformly and deactivate them since the discharging product is an insulator. The other one is the particle-type growth (i.e. toroid) with preferential Li and O_2 binding not on the catalyst surface, but on the discharging product. The catalyst surface will have an active open place even though the numerous discharging process with particle-type growth. We also tried to check which type of growth is dominant for our systems. When we explored the stable structures of adsorbed LiO_2 and Li_2O_2, could not find any differences. However, the third reaction step formation of Li_2O_3 from Li_2O_2 showed a clear difference that we can claim one is the film-type growth and the other one is the particle-type growth. As shown in Fig. 4b, extra Li and O_2(g) can make entirely different Li_3O_4 structures. Two oxygen atoms are strongly bound with carbon atoms when Li_2O_2 binds with catalysts. When the Li_3O_4 is formed, O_2(g) can be activated by either graphene or Li atoms. If the O_2(g) strongly interacts with graphene, then it will make film-type Li_3O_4. On the other hand, O_2(g) is positioned on top of the Li atoms, and then the Li_3O_4 structure is rearranged to a particle shape as only two oxygen atoms are bound to the graphene. To return to the binding energy of adsorbates, we calculated the binding energies of film-type and particle-type Li_3O_4, and we found many interesting points. As we discussed, Co@C showed the best performance among the monometallic systems. Furthermore, only Co@C showed stronger particle-type Li_3O_4 binding energy than film-type one (see Fig. 4a), another interesting point is all the random alloy systems preferred particle-type growth. Lastly, FeCo@C showed the weakest Li_3O_4 binding energy among all the systems we considered in this study. Eventually, this weak binding energy of Li_3O_4 drove the system to the best catalyst.

As we explained, the strength of binding energy is critical in Li-air batteries since the overly stable discharging product is the problem. According to binding energy calculation, FeCo@C preferred particle-type growth and had weak binding energy, that is, we can easily predict that FeCo@C would have good catalytic performance. However, when you see the overall potential difference from the reaction energy diagram on the random alloy systems in Fig. S4, FeCo@C is not the one with the highest activity, and the activity difference between the systems is negligible (below 10 mV). We must see the individual potential difference to understand what happened during the reaction (see Fig. 4d to f). The discharging potential in blue color does not change with the system or Li_2O_2 formation and decomposition order, so the charging or decomposition of stable Li_2O_2 is the main key to pursuing the high activity. An overly stable Li_2O_2 intermediate makes the discharging reaction fast. Furthermore, the discharging potential showed an almost flat line along with the capacity from our previous study. [52] Above all, you can find a dramatic activity increase in FeCo@C compared to others. Around 40 ~ 60 mV improvement was observed, and it is the opposite result we found in the previous overall potential difference data. To return to the suggestion that we need individual potential differences, we can see solid proof through the random alloy calculation result. Since

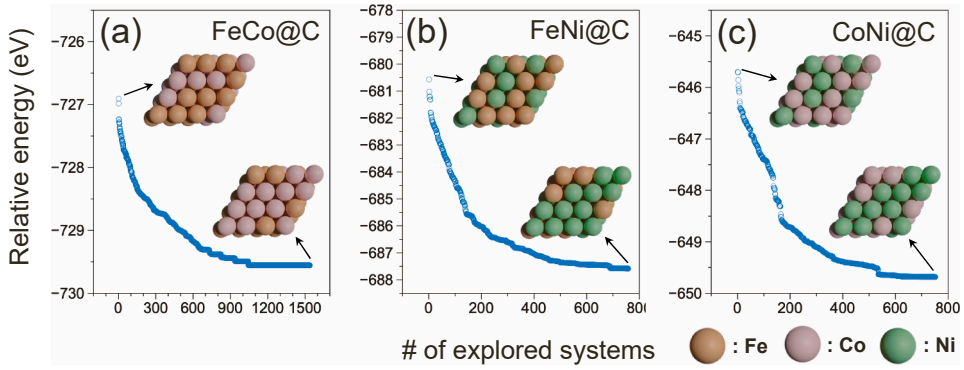

Fig. 3. The number of explored systems via the GA method for the (a) FeCo@C, (b) FeNi@C, and (c) CoNi@C. The structure illustration in each figure showed the highest and lowest energy structure without graphene encapsulation.

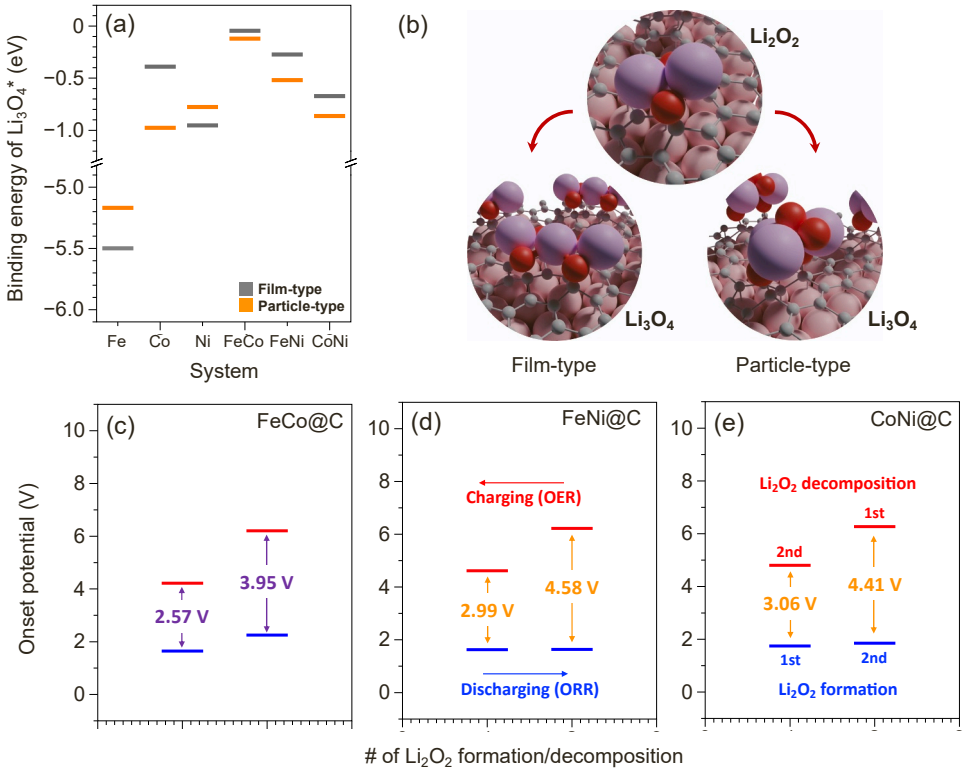

Fig. 4. (a) Different configurations of intermediate binding on each system, (b) illustrations of film-type binding and particle-type Li_3O_4 binding configurations from Li_2O_2, the individual potential difference along with Li_2O_2 formation and decomposition on the (c) FeCo@C, (d) FeNi@C, and (e) CoNi@C.

Co@C was the best catalyst among the monometallic systems, we can simply predict the system with a Co-rich surface can have at least similar activity with the Co@C system, but how the FeCo@C showed the best performance, not the CoNi@C system. According to previous calculations, any active elements at the sub-surface layer weaken the binding energy at the surface. In the case of Pt_3Ni catalyst for oxygen reduction reaction, we usually assumed that the surface will be fully covered with thin Pt skin due to the poor stability of Ni elements. The binding energy of key adsorbate O or OH becomes weaker than that of Pt toward the top of the volcano curve. [57,58] The reactive elements at the sub-surface will strongly attract the electrons from the neighbor including surface atoms, and the reactivity of the surface atom will be suppressed. In other words, we can control the strength of binding energy with or without the surface layer (specifically the graphene layer) and even the performance of the Li-air batteries.

In summary, we found that there are two distinguished discharging product growth mechanisms and our best system FeCo@C preferred particle-type growth and the weakest binding energy. We also found that the overall potential difference is no more helpful to determine the actual catalytic activity of Li-air battery and need the individual potential difference data to get reliable results.

4. Conclusion

In this study, we investigated the graphene-encapsulated monometallic (Fe, Co, and Ni) and bimetallic random alloys (FeCo, FeNi, and CoNi) systems for their potential application as catalysts in Li-air batteries. Our calculations and analyses focused on evaluating the catalytic activity of these systems. Among the monometallic systems, the Co@C catalyst demonstrated the highest performance due to its particle-type growth of the discharging product, which was found to be more advantageous than film-type growth, along with moderate intermediate binding energy. To identify stable random alloy systems, we systematically explored approximately 800–1200 structures using the genetic algorithm (GA) method. As a result, we discovered the stable FeCo@C catalyst with a Co-rich surface, FeNi@C catalyst with a Ni-rich surface, and CoNi@C catalyst with a Ni-rich surface. Although the catalyst surfaces were predominantly composed of specific elements, the binding of intermediates occurred at ensemble sites involving two elements. The FeCo@C catalyst, among both monometallic and bimetallic systems, demonstrated superior performance. This catalyst exhibited a preference for particle-type growth and possessed the weakest binding energy for Li_3O_4, leading to enhanced catalytic activity. Furthermore, we analyzed the overall potential difference from the reaction energy diagram and the individual potential differences during the Li_2O_2 formation and decomposition process. Interestingly, the catalytic performance appeared to deviate from our initial assumptions, prompting us to conclude that comparing individual potential differences in Li-air battery studies is crucial for preserving detailed information and maintaining predictive capabilities for suggesting new catalysts. In summary, our study provides insights into the performance of graphene-encapsulated monometallic and bimetallic catalysts in Li-air batteries. The Co@C catalyst exhibited the most promising performance among the monometallic systems, while the FeCo@C catalyst demonstrated superior activity among both monometallic and bimetallic systems. Our findings highlight the importance of considering individual potential differences and preserving detailed information to advance the development of efficient catalysts for Li-air battery applications.

CRediT authorship contribution statement

Hyunwoo Ha: Software, Investigation. **Changsoo Lee**: Methodology, Formal analysis. **Joon Sik Park**: Writing – review & editing, Visualization. **Choong-Heui Chung**: Writing – review & editing, Visualization. **Sangyeob Lee**: Funding acquisition, Resources. **Graeme Henkelman**: Supervision, Resources. **Kihyun Shin**: Project administration, Supervision, Writing – original draft.

Declaration of Competing Interest

The authors declare that they have no known competing financial interests or personal relationships that could have appeared to influence the work reported in this paper.

Data availability

No data was used for the research described in the article.

Acknowledgments

This result was supported by the "Regional Innovation Strategy (RIS)" through the National Research Foundation of Korea (NRF) funded by the Ministry of Education (MOE) (2021RIS-004). This work was also supported by the research fund of Chungnam National University. DFT calculation used Anvil at Purdue University through the allocation CHE190010 from the Advanced Cyberinfrastructure Coordination Ecosystem: Services & Support (ACCESS) program.

Appendix A. Supporting information

Supplementary data associated with this article can be found in the online version at doi:10.1016/j.cattod.2023.114303.

References

[1] R. Lin, Y. Wang, Q. Lu, B. Tang, J. Li, H. Gao, Y. Gao, H. Li, C. Ding, J. Wen, P. Wu, C. Liu, S. Zhao, K. Xiao, Z. Liu, C. Ma, Y. Deng, L. Li, F. Fan, H. Tan, All-perovskite tandem solar cells with 3D/3D bilayer perovskite heterojunction, Nature (2023), https://doi.org/10.1038/s41586-023-06278-z.

[2] F. Li, A. Thevenon, A. Rosas-Hernández, Z. Wang, Y. Li, C.M. Gabardo, A. Ozden, C. T. Dinh, J. Li, Y. Wang, J.P. Edwards, Y. Xu, C. McCallum, L. Tao, Z.-Q. Liang, M. Luo, X. Wang, H. Li, C.P. O'Brien, C.-S. Tan, D.-H. Nam, R. Quintero-Bermudez, T.-T. Zhuang, Y.C. Li, Z. Han, R.D. Britt, D. Sinton, T. Agapie, J.C. Peters, E. H. Sargent, Molecular tuning of CO_2-to-ethylene conversion, Nature 577 (2020) 509–513, https://doi.org/10.1038/s41586-019-1782-2.

[3] P. Garrido-Barros, J. Derosa, M.J. Chalkley, J.C. Peters, Tandem electrocatalytic N2 fixation via proton-coupled electron transfer, Nature 609 (2022) 71–76, https://doi.org/10.1038/s41586-022-05011-6.

[4] Y. Park, K. Shin, C. Lee, S.-Y. Lee, Y.-K. Lee, C.-H. Kim, H.-S. Cho, G. Henkelman, H. M. Lee, Iterative redox activation promotes interfacial synergy in an Ag/CuxO catalyst for oxygen reduction, Chem. Eng. J. 446 (2022), 136966, https://doi.org/10.1016/j.cej.2022.136966.

[5] Y.-J. Rho, B. Kim, K. Shin, G. Henkelman, W.-H. Ryu, Atomically miniaturized bi-phase IrOx/Ir catalysts loaded on N-doped carbon nanotubes for high-performance Li–CO_2 batteries, J. Mater. Chem. A. 10 (2022) 19710–19721, https://doi.org/10.1039/D2TA02234F.

[6] C. Lee, K. Shin, Y. Park, Y.H. Yun, G. Doo, G.H. Jung, M. Kim, W.-C. Cho, C.-H. Kim, H.M. Lee, H.Y. Kim, S. Lee, G. Henkelman, H.-S. Cho, Catalyst-Support Interactions in Zr2ON2-Supported IrOx electrocatalysts to break the trade-off relationship between the activity and stability in the acidic oxygen evolution reaction, Adv. Funct. Mater. n/a (2023) 2301557, https://doi.org/10.1002/adfm.202301557.

[7] O. Schmidt, A. Hawkes, A. Gambhir, I. Staffell, The future cost of electrical energy storage based on experience rates, Nat. Energy 2 (2017) 17110, https://doi.org/10.1038/nenergy.2017.110.

[8] J.-W. Jung, C.-L. Lee, S. Yu, I.-D. Kim, Electrospun nanofibers as a platform for advanced secondary batteries: a comprehensive review, J. Mater. Chem. A 4 (2016) 703–750, https://doi.org/10.1039/C5TA06844D.

[9] J.W. Choi, D. Aurbach, Promise and reality of post-lithium-ion batteries with high energy densities, Nat. Rev. Mater. 1 (2016) 16013, https://doi.org/10.1038/natrevmats.2016.13.

[10] L. Yue, C. Ma, S. Yan, Z. Wu, W. Zhao, Q. Liu, Y. Luo, B. Zhong, F. Zhang, Y. Liu, A. A. Alshehri, K.A. Alzahrani, X. Guo, X. Sun, Improving the intrinsic electronic conductivity of NiMoO4 anodes by phosphorous doping for high lithium storage, Nano Res 15 (2022) 186–194, https://doi.org/10.1007/s12274-021-3455-3.

[11] J.-S. Lee, K. Shin, S.-Y. Jun, S. Kim, W.-H. Ryu, Dual-functional vinylpyrrolidone electrolyte additive as anode surface leveler and cathode catalyst for lithium Metal-Oxygen batteries, Chem. Eng. J. 458 (2023), 141383, https://doi.org/10.1016/j.cej.2023.141383.

[12] S.-Y. Jun, K. Shin, J.-S. Lee, S. Kim, J. Chun, W.-H. Ryu, Molecular dipoles as a surface flattening and interface stabilizing agent for lithium-metal batteries, Adv. Sci. n/a (2023) 2301426, https://doi.org/10.1002/advs.202301426.

[13] J. Lu, Y. Jung Lee, X. Luo, K. Chun Lau, M. Asadi, H.-H. Wang, S. Brombosz, J. Wen, D. Zhai, Z. Chen, D.J. Miller, Y. Sub Jeong, J.-B. Park, Z. Zak Fang, B. Kumar, A. Salehi-Khojin, Y.-K. Sun, L.A. Curtiss, K. Amine, A lithium–oxygen battery based on lithium superoxide, Nature 529 (2016) 377–382, https://doi.org/10.1038/nature16484.

[14] X. Yao, Q. Dong, Q. Cheng, D. Wang, Why Do Lithium-Oxygen Batteries Fail: parasitic chemical reactions and their synergistic effect, Angew. Chem. Int. Ed. 55 (2016) 11344–11353, https://doi.org/10.1002/anie.201601783.

[15] G.-Y. Kim, J. Lee, Y.-J. Rho, W.-H. Kim, M. Kim, J.-H. Ahn, W.-H. Ryu, Rhenium oxide/sulfide binary phase flakes decorated on nanofiber support for enhanced activation of electrochemical conversion reactions, Chem. Eng. J. 446 (2022), 136951, https://doi.org/10.1016/j.cej.2022.136951.

[16] G.-Y. Kim, K.R. Yoon, K. Shin, J.-W. Jung, G. Henkelman, W.-H. Ryu, Black tungsten oxide nanofiber as a robust support for metal catalysts: high catalyst loading for electrochemical oxygen Reduction, Small 17 (2021) 2103755, https://doi.org/10.1002/smll.202103755.

[17] W.-H. Ryu, F.S. Gittleson, M. Schwab, T. Goh, A.D. Taylor, A mesoporous catalytic membrane architecture for lithium–oxygen battery systems, Nano Lett. 15 (2015) 434–441, https://doi.org/10.1021/nl503760n.

[18] W.-H. Ryu, F.S. Gittleson, J. Li, X. Tong, A.D. Taylor, A new design strategy for observing lithium oxide growth-evolution interactions using geometric catalyst positioning, Nano Lett. 16 (2016) 4799–4806, https://doi.org/10.1021/acs.nanolett.6b00856.

[19] K.R. Yoon, D.S. Kim, W.-H. Ryu, S.H. Song, D.-Y. Youn, J.-W. Jung, S. Jeon, Y. J. Park, I.-D. Kim, Tailored combination of low dimensional catalysts for efficient oxygen reduction and evolution in Li–O2 batteries, ChemSusChem 9 (2016) 2080–2088, https://doi.org/10.1002/cssc.201600341.

[20] K.S. Kim, Y.J. Park, Catalytic properties of Co3O4 nanoparticles for rechargeable Li/air batteries, Nanoscale Res. Lett. 7 (2012) 47, https://doi.org/10.1186/1556-276X-7-47.

[21] P.-F. Zhang, H.-Y. Zhuo, Y.-Y. Dong, Y. Zhou, Y.-W. Li, H.-G. Hao, D.-C. Li, W.-J. Shi, S.-Y. Zeng, S.-L. Xu, X.-J. Kong, Y.-J. Wu, J.-S. Zhao, S. Zhao, J.-T. Li, Pt Nanoparticles Confined in a 3D Porous FeNC Matrix as efficient catalysts for rechargeable Li-CO_2/O2 batteries, ACS Appl. Mater. Interfaces 15 (2023) 2940–2950, https://doi.org/10.1021/acsami.2c18857.

[22] T. Wang, F. Yin, Y. Fang, C. Sun, Waste cigarette butts-derived nitrogen-doped carbon fibers loaded with Ru nanoparticles as an efficient cathode catalyst for lithium-oxygen batteries, ACS Sustain. Chem. Eng. (2023), https://doi.org/10.1021/acssuschemeng.3c02050.

[23] E.Y. Choi, D.E. Kim, S.Y. Lee, C.B. Park, C.K. Kim, Cobalt nanoparticles-encapsulated holey nitrogen-doped carbon nanotubes for stable and efficient oxygen reduction and evolution reactions in rechargeable Zn-air batteries, Appl. Catal. B Environ. 325 (2023), 122386, https://doi.org/10.1016/j.apcatb.2023.122386.

[24] J.G. Kim, Y. Noh, Y. Kim, Pyrochlore LaSrSn2O7 nanoparticles anchored on carbon nanofibers as bifunctional catalysts for an efficient Li-O2 battery, J. Energy Storage 66 (2023), 107329, https://doi.org/10.1016/j.est.2023.107329.

[25] T. Wang, J. Liang, Z. Zhao, S. Li, G. Lu, Z. Xia, C. Wang, J. Luo, J. Han, C. Ma, Y. Huang, Q. Li, Sub-6 nm fully ordered L10-Pt–Ni–Co nanoparticles enhance oxygen reduction via co doping induced ferromagnetism enhancement and optimized surface strain, Adv. Energy Mater. 9 (2019) 1803771, https://doi.org/10.1002/aenm.201803771.

[26] S.H. Krishna, A. Goswami, Y. Wang, C.B. Jones, D.P. Dean, J.T. Miller, W. F. Schneider, R. Gounder, Influence of framework Al density in chabazite zeolites on copper ion mobility and reactivity during NOx selective catalytic reduction with NH3, Nat. Catal. 6 (2023) 276–285, https://doi.org/10.1038/s41929-023-00932-5.

[27] K. Pan, M. Li, W. Wang, S. Xing, Y. Dou, S. Gao, Z. Zhang, Z. Zhou, A leap by the rise of solid-state electrolytes for Li-air batteries, Green. Energy Environ. (2023), https://doi.org/10.1016/j.gee.2023.02.010.

[28] R. Cao, K. Chen, J. Liu, G. Huang, W. Liu, X. Zhang, Li–air batteries: air stability of lithium metal anodes, Sci. China Chem. (2023), https://doi.org/10.1007/s11426-023-1581-2.

[29] C. Lee, K. Shin, Y.J. Lee, C. Jung, H.M. Lee, Effects of shell thickness on Ag-Cu<inf>2</inf>O core-shell nanoparticles with bumpy structures for enhancing photocatalytic activity and stability, Catal. Today 303 (2018), https://doi.org/10.1016/j.cattod.2017.08.016.

[30] A. Galyamova, K. Shin, G. Henkelman, R.M. Crooks, Effect of TiO<inf>x</inf> substrate interactions on the electrocatalytic oxygen reduction reaction at au nanoparticles, J. Phys. Chem. C. 124 (2020), https://doi.org/10.1021/acs.jpcc.0c02754.

[31] K. Kawashima, K. Shin, B. Wygant, J.-H. Kim, C. Cao, J. Lin, Y.J. Son, yang liu, G. Henkelman, C. Mullins, Cobalt Metal-Cobalt Carbide Composite Microspheres for Water Reduction Electrocatalysis, ACS Appl. Energy Mater. 3 (n.d.) 3909–3918. ⟨https://doi.org/10.1021/acsaem.0c00321⟩.

[32] K. Bang, K. Shin, M.S. Ryu, S. Kwon, H.M. Lee, Titanium-promoted Au-Ti bimetallic nanoparticle catalysts for CO oxidation: a theoretical approach, Catal. Today 265 (2016), https://doi.org/10.1016/j.cattod.2015.09.040.

[33] K. Shin, L. Zhang, H. An, H. Ha, M. Yoo, H.M. Lee, G. Henkelman, H.Y. Kim, Interface engineering for a rational design of poison-free bimetallic CO oxidation catalysts, Nanoscale 9 (2017), https://doi.org/10.1039/c7nr01382e.

[34] K. Huang, K. Shin, G. Henkelman, R.M. Crooks, Correlating surface structures and electrochemical activity using shape-controlled single-Pt nanoparticles, ACS Nano 15 (2021) 17926–17937, https://doi.org/10.1021/acsnano.1c06281.

[35] E.-T. Yun, S.-W. Park, H.J. Shin, H. Lee, D.-W. Kim, J. Lee, Peroxymonosulfate activation by carbon-encapsulated metal nanoparticles: switching the primary reaction route and increasing chemical stability, Appl. Catal. B Environ. 279 (2020), 119360, https://doi.org/10.1016/j.apcatb.2020.119360.

[36] J.-H. Jang, A.A. Jeffery, J. Min, N. Jung, S.J. Yoo, Emerging carbon shell-encapsulated metal nanocatalysts for fuel cells and water electrolysis, Nanoscale 13 (2021) 15116–15141, https://doi.org/10.1039/D1NR01328A.

[37] J.M. Yoo, H. Shin, D.Y. Chung, Y.-E. Sung, Carbon shell on active nanocatalyst for stable electrocatalysis, Acc. Chem. Res. 55 (2022) 1278–1289, https://doi.org/10.1021/acs.accounts.1c00727.
[38] Y. Hu, Y. Lu, X. Zhao, T. Shen, T. Zhao, M. Gong, K. Chen, C. Lai, J. Zhang, H.L. Xin, D. Wang, Highly active N-doped carbon encapsulated Pd-Fe intermetallic nanoparticles for the oxygen reduction reaction, Nano Res 13 (2020) 2365–2370, https://doi.org/10.1007/s12274-020-2856-z.
[39] J.Y. Park, M.A. Kim, S.J. Lee, J. Jung, H.M. Jang, P.P. Upare, Y.K. Hwang, J.-S. Chang, J.K. Park, Preparation and characterization of carbon-encapsulated iron nanoparticles and their catalytic activity in the hydrogenation of levulinic acid, J. Mater. Sci. 50 (2015) 334–343, https://doi.org/10.1007/s10853-014-8592-6.
[40] G. Kresse, J. Hafner, Ab initio molecular dynamics for liquid metals, Phys. Rev. B 47 (1993) 558–561, https://doi.org/10.1103/PhysRevB.47.558.
[41] G. Kresse, J. Furthmüller, Efficient iterative schemes for ab initio total-energy calculations using a plane-wave basis set, Phys. Rev. B. 54 (1996) 11169–11186, https://doi.org/10.1103/PhysRevB.54.11169.
[42] G. Kresse, J. Furthmüller, Efficiency of ab-initio total energy calculations for metals and semiconductors using a plane-wave basis set, Comput. Mater. Sci. 6 (1996) 15–50, https://doi.org/10.1016/0927-0256(96)00008-0.
[43] G. Kresse, D. Joubert, From ultrasoft pseudopotentials to the projector augmented-wave method, Phys. Rev. B 59 (1999) 1758–1775, https://doi.org/10.1103/PhysRevB.59.1758.
[44] B. Hammer, L.B. Hansen, J.K. Nørskov, Improved adsorption energetics within density-functional theory using revised Perdew-Burke-Ernzerhof functionals, Phys. Rev. B 59 (1999) 7413–7421, https://doi.org/10.1103/PhysRevB.59.7413.
[45] J.P. Perdew, K. Burke, M. Ernzerhof, Generalized gradient approximation made simple, Phys. Rev. Lett. 77 (1996) 3865–3868, https://doi.org/10.1103/PhysRevLett.77.3865.
[46] Y. Zhang, W. Yang, Comment on Generalized Gradient Approximation Made Simple, Phys. Rev. Lett. 80 (1998) 890, https://doi.org/10.1103/PhysRevLett.80.890.
[47] L.B. Vilhelmsen, B. Hammer, Systematic Study of ${\mathrm{Au}}_{6}$ to ${\mathrm{Au}}_{12}$ Gold Clusters on MgO(100) F Centers Using Density-Functional Theory, Phys. Rev. Lett. 108 (2012), 126101, https://doi.org/10.1103/PhysRevLett.108.126101.
[48] L.B. Vilhelmsen, B. Hammer, A genetic algorithm for first principles global structure optimization of supported nano structures, J. Chem. Phys. 141 (2014) 44711, https://doi.org/10.1063/1.4886337.
[49] A.A. Peterson, F. Abild-Pedersen, F. Studt, J. Rossmeisl, J.K. Nørskov, How copper catalyzes the electroreduction of carbon dioxide into hydrocarbon fuels, Energy Environ. Sci. 3 (2010) 1311–1315, https://doi.org/10.1039/C0EE00071J.
[50] H. Khani, N.S. Grundish, D.O. Wipf, J.B. Goodenough, Graphitic-Shell encapsulation of metal electrocatalysts for oxygen evolution, oxygen reduction, and hydrogen evolution in alkaline solution, Adv. Energy Mater. 10 (2020) 1903215, https://doi.org/10.1002/aenm.201903215.
[51] R. Nandan, P. Pandey, A. Gautam, O.Y. Bisen, K. Chattopadhyay, M.-M. Titirici, K. K. Nanda, Atomic arrangement modulation in CoFe nanoparticles encapsulated in n-doped carbon nanostructures for efficient oxygen reduction reaction, ACS Appl. Mater. Interfaces 13 (2021) 3771–3781, https://doi.org/10.1021/acsami.0c16937.
[52] K.R. Yoon, K. Shin, J. Park, S.-H. Cho, C. Kim, J. Jung, J.Y. Cheong, H.R. Byon, H. M. Lee, I.-D. Kim, Brush-Like Cobalt Nitride Anchored Carbon Nanofiber Membrane: Current Collector-Catalyst Integrated Cathode for Long Cycle Li–O_2 Batteries, ACS Nano. 12 (n.d.) 128–139. ⟨https://doi.org/10.1021/acsnano.7b03794⟩.
[53] B.G. Kim, H.-J. Kim, S. Back, K.W. Nam, Y. Jung, Y.-K. Han, J.W. Choi, Improved reversibility in lithium-oxygen battery: understanding elementary reactions and surface charge engineering of metal alloy catalyst, Sci. Rep. 4 (2014) 4225, https://doi.org/10.1038/srep04225.
[54] J.S. Hummelshøj, J. Blomqvist, S. Datta, T. Vegge, J. Rossmeisl, K.S. Thygesen, A. C. Luntz, K.W. Jacobsen, J.K. Nørskov, Communications: elementary oxygen electrode reactions in the aprotic Li-air battery, J. Chem. Phys. 132 (2010) 71101, https://doi.org/10.1063/1.3298994.
[55] J.S.G. Mýrdal, T. Vegge, Selective poisoning of Li–air batteries for increased discharge capacity, RSC Adv. 4 (2014) 15671–15674, https://doi.org/10.1039/C3RA47390B.
[56] X. Huang, Z. Zhao, L. Cao, Y. Chen, E. Zhu, Z. Lin, M. Li, A. Yan, A. Zettl, Y. M. Wang, X. Duan, T. Mueller, Y. Huang, High-performance transition metal–doped Pt3Ni octahedra for oxygen reduction reaction, Science 348 (80) (2015) 1230–1234, https://doi.org/10.1126/science.aaa8765.
[57] J. Lim, K. Shin, J. Bak, J. Roh, S. Lee, G. Henkelman, E. Cho, Outstanding Oxygen Reduction Reaction Catalytic Performance of In–PtNi Octahedral Nanoparticles Designed via Computational Dopant Screening, Chem. Mater. 33 (n.d.) 8895–8903. ⟨https://doi.org/10.1021/acs.chemmater.1c03196⟩.
[58] J.T.L. Gamler, K. Shin, H.M. Ashberry, Y. Chen, S.L.A. Bueno, Y. Tang, G. Henkelman, S.E. Skrabalak, Intermetallic Pd<inf>3</inf>Pb nanocubes with high selectivity for the 4-electron oxygen reduction reaction pathway, Nanoscale 12 (2020), https://doi.org/10.1039/c9nr09759g.
[59] J.-J. Xu, Z.-W. Chang, Y. Wang, D.-P. Liu, Y. Zhang, X.-B. Zhang, Cathode surface-induced, solvation-mediated, micrometer-sized Li2O2 Cycling for Li–O2 batteries, Adv. Mater. 28 (2016) 9620–9628, https://doi.org/10.1002/adma.201603454.